

---

# CMS Physics Analysis Summary

---

Contact: cms-pag-conveners-smp@cern.ch

2013/07/19

## Measurement of the 3-jet mass cross section in $pp$ collisions at 7 TeV and determination of the strong coupling constant from 3-jet masses in the TeV range

The CMS Collaboration

### Abstract

This study presents a measurement of the double-differential cross section of 3-jet events at a center-of-mass energy of  $\sqrt{s} = 7$  TeV, using data corresponding to an integrated luminosity of  $5 \text{ fb}^{-1}$  collected with the CMS detector in 2011. The cross section is measured as a function of the invariant mass and maximum rapidity of the 3-jet system and is unfolded for detector effects. A comparison between the measurement and the prediction from perturbative QCD at next-to-leading order is performed. Within uncertainties, data and theory are in agreement. The sensitivity of the observable to parameters of the theory like the parton distribution functions of the proton and the strong coupling  $\alpha_s$  is studied. A fit of all data points at central rapidity gives the value of the strong coupling at the scale of the Z boson mass to be  $\alpha_s(M_Z) = 0.1160 \pm_{0.0023}^{0.0025} \text{ (exp, PDF, NP)} \pm_{0.0021}^{0.0068} \text{ (scale)}$ .



## 1 Introduction

A key characteristic of high-energetic proton-proton collisions at the Large Hadron Collider (LHC) is the abundant production of jets and multi-jet events. At high transverse momenta such events are described by quantum chromodynamics (QCD) in terms of parton-parton scattering. The signatures of lowest complexity, where the leading-order (LO) prediction in perturbative QCD (pQCD) is proportional to  $\alpha_s^2$ , have been measured previously in the form of inclusive jet  $p_T$  and dijet mass cross sections [1–4]. In this paper, the measurement of the double-differential 3-jet mass cross section is reported as a function of the mass  $m_3$  and the maximum rapidity  $y_{\max}$  of the 3-jet system with

$$m_3^2 = (p_1 + p_2 + p_3)^2 \quad (1)$$

$$y_{\max} = \text{sign}(|\max(y_1, y_2, y_3)| - |\min(y_1, y_2, y_3)|) \cdot \max(|y_1|, |y_2|, |y_3|) \quad (2)$$

where  $p_i$  and  $y_i$  are the four-momentum and rapidity of the  $i$ -th jet leading in  $p_T$ . For this observable the LO process is proportional to  $\alpha_s^3$  and theory predictions are available up to next-to-leading order (NLO) such that precise comparisons to data are possible. Constraints on the parton distribution functions (PDFs) of the proton are studied and the strong coupling  $\alpha_s$  is extracted from the  $|y_{\max}| < 1$  bin, which exhibits the smallest experimental uncertainty. A previous study on the 3-jet mass was published by the D0 Collaboration [5].

The data were recorded by the Compact Muon Solenoid (CMS) detector at the LHC during the 2011 run and correspond to an integrated luminosity of  $5.0 \text{ fb}^{-1}$ . CMS uses a right-handed coordinate system, with the origin at the nominal interaction point, the  $x$  axis pointing to the centre of the LHC, the  $y$  axis pointing up (perpendicular to the LHC plane), and the  $z$  axis along the anticlockwise-beam direction. The polar angle  $\theta$  is measured from the positive  $z$  axis and the azimuthal angle  $\phi$  is measured in the  $x$ - $y$  plane. The rapidity  $y$  is defined as  $y = 1/2 \cdot \ln((E + p_z)/(E - p_z))$  and the pseudorapidity as  $\eta = -\ln \tan(\theta/2)$ . Events are studied where at least three jets are found up to a rapidity of  $|y| = 3$  that are above a minimal  $p_T$  threshold of 100 GeV. The measured cross sections are corrected for detector effects.

## 2 Apparatus and event reconstruction

The central feature of the CMS detector is a superconducting solenoid of 6 m internal diameter, providing a magnetic field of 3.8 T. Within the superconducting solenoid volume are a silicon pixel and strip tracker, a lead tungstate crystal electromagnetic calorimeter (ECAL), and a brass/scintillator hadron calorimeter (HCAL). Muons are measured in gas-ionization detectors embedded in the steel return yoke outside the solenoid. Extensive forward calorimetry complements the coverage provided by the barrel and endcap detectors.

In the region  $|\eta| < 1.74$ , the HCAL cells have widths of 0.087 in pseudorapidity and 0.087 in azimuth. In the  $\eta$ - $\phi$  plane, and for  $|\eta| < 1.48$ , the HCAL cells map on to  $5 \times 5$  ECAL crystals arrays to form calorimeter towers projecting radially outwards from close to the nominal interaction point. At larger values of  $|\eta|$ , the size of the towers increases and the matching ECAL arrays contain fewer crystals. Within each tower, the energy deposits in ECAL and HCAL cells are summed to define the calorimeter tower energies, subsequently used to provide energies and directions to the event reconstruction. The ECAL has an energy resolution of better than 0.5% for unconverted photons with transverse energies above 100 GeV. The HCAL, when combined with the ECAL, measures jets with a resolution  $\Delta E/E \approx 100\%/\sqrt{E [\text{GeV}]} \oplus 5\%$ . A more

detailed description of the CMS apparatus can be found in Ref. [6].

The first level (L1) of the CMS trigger system, composed of custom hardware processors, uses information from the calorimeters and muon detectors to select the most interesting events in a fixed time interval of less than  $4\mu\text{s}$ . The High Level Trigger (HLT) processor farm further decreases the event rate from around 100 kHz to around 300 Hz, before data storage.

The global event reconstruction (also called particle-flow event reconstruction [7, 8]) consists in reconstructing and identifying each single particle with an optimized combination of all sub-detector information. The energy of photons is directly obtained from the ECAL measurement, corrected for zero-suppression effects. The energy of electrons is determined from a combination of the track momentum at the main interaction vertex, the corresponding ECAL cluster energy, and the energy sum of all bremsstrahlung photons attached to the track. The energy of muons is obtained from the corresponding track momentum. The energy of charged hadrons is determined from a combination of the track momentum and the corresponding ECAL and HCAL energy, corrected for zero-suppression effects, and calibrated for the nonlinear response of the calorimeters. Finally the energy of neutral hadrons is obtained from the corresponding calibrated ECAL and HCAL energy.

For each event, the reconstructed particle candidates are clustered into hadronic jets with the infrared- and collinear-safe anti- $k_T$  algorithm [9] as implemented in the FASTJET package [10] with a jet size parameter of  $R = 0.7$ . Jet momentum is determined as the vectorial sum of all constituent momenta in the jet, and is found in the simulation to be within 5 to 10% of the true momentum over the whole  $p_T$  spectrum and detector acceptance. An offset correction is applied to take into account the extra energy clustered into jets due to additional proton-proton interactions within the same or neighbouring bunch crossings (pile-up). Jet energy corrections are derived from the simulation, and are confirmed with in situ measurements with the energy balance of dijet, photon+jet and Z+jet events [11]. Additional selection criteria are applied to each event to remove spurious jet-like features originating from isolated noise patterns in certain HCAL regions.

### 3 Event selection

This analysis is based on proton-proton collisions collected at a center-of-mass energy of 7 TeV by the CMS experiment. The dataset contains all events, which were triggered by one of the CMS single-jet triggers. A single-jet trigger accepts events if at least one reconstructed jet surpasses a transverse momentum threshold. During the investigated data taking period triggers with nine different thresholds ranging from 30 up to 370 GeV were employed.

Because one such single-jet trigger is unable to reach full efficiency as a function of the 3-jet mass, it is necessary to combine multiple single-jet triggers to reconstruct the complete 3-jet mass distribution. For each trigger path, the turnon-point above which the trigger is more than 99% efficient is determined. The transverse momentum interval covered by a single-jet trigger starts at the corresponding turnon-point and ends at the turnon-point of the trigger with the next highest threshold. The trigger with the highest threshold is used for all events above its turnon-point. The 3-jet mass measured from events in these disjoint phase-space regions is added together, taking trigger prescales into account.

The recorded events are filtered with tracking based cuts [12] to remove interactions between the circulating proton bunches and residual gas particles or the beam collimators. To further reject beam backgrounds and off-center parasitic bunch crossings, vertex selection cuts are ap-

plied [12]. To enhance the QCD event purity, events where the missing transverse energy  $E_T^{\text{miss}}$  amounts to more than 30% of the measured total transverse energy are removed.

The jet identification (jet ID) selection criteria [13] were developed in order to reject pure noise or noise enhanced jets, while keeping more than 99% of physical jets above 10 GeV. Contrary to the previous selection criteria, which rejected complete events, the jet ID operates on individual jets. While it is possible that all jets in an event fail the jet ID criteria, having jets which fail the jet identification does not imply that the event should be discarded. The jet ID applied to the particle flow jets requires that each jet should contain at least two particles, one of which is a charged hadron. In addition, the jet energy fraction carried by neutral hadrons and photons must be less than 90%. These criteria have an efficiency greater than 99% for physical jets.

Furthermore only jets, whose transverse momentum exceeds 100 GeV and which lie in the central detector region with  $|y| < 3$  are taken into account. The event is rejected if less than three jets fulfill the jet ID and detector acceptance requirements.

## 4 Measurement

The double-differential 3-jet mass cross section is measured as a function of the invariant mass  $m_3$  and the maximum rapidity  $y_{\text{max}}$  of the three jets with the highest transverse momentum in the event:

$$\frac{d^2\sigma}{dm_3 dy_{\text{max}}} = \frac{1}{\epsilon \mathcal{L}_{\text{eff}}} \frac{N}{\Delta m_3 (2 \cdot \Delta |y|_{\text{max}})} \quad (3)$$

Here,  $\epsilon$  is the product of the selection efficiencies in this bin,  $\mathcal{L}_{\text{eff}}$  is the integrated luminosity and  $N$  is the number of events in the bin. The width of the 3-jet mass bins is based on the 3-jet mass resolution, which is derived from a full detector simulation and which progressively increases with  $m_3$ . The phase space is split into an inner  $|y|_{\text{max}} < 1$  and an outer  $1 \leq |y|_{\text{max}} < 2$  rapidity region. The bin widths in  $y_{\text{max}}$  are then equal to two.

Detector effects like limited acceptance and finite resolution cause differences between the measured and true 3-jet mass distributions. In order to remove these influences, the measurement is corrected with the iterative D'Agostini unfolding algorithm [14] with four iterations. Response matrices for the unfolding algorithm are derived from detector simulation using the two event generators PYTHIA version 6.4.22 [15] tune Z2 [16, 17] and HERWIG++ version 2.4.2 [18] with the default tune. Differences in the unfolding result account for uncertainties caused by the assumptions in modelling the underlying physics by these event generators. Additional uncertainties dealt with in the unfolding procedure are determined from toy experiments, where the data input and the response matrix are varied within the limits of their statistical precision. The unfolding result corresponds to the sample mean, while the statistical uncertainty, which is propagated through the unfolding procedure, is given by the toy sample covariance. The variation of the input data leads to the statistical uncertainty of the unfolded cross section, while the variation of the response matrix is an additional uncertainty inherent to the unfolding technique because of the limited size of simulated samples.

A second origin of systematic effects is the determination of the jet energies. In CMS the jet energy uncertainty is evaluated via 16 independent sources as described in Ref. [4]. The four components of the jet energy uncertainty most important for the 3-jet mass measurement are the uncertainty on the absolute jet energy scale, the uncertainty due to the high- $p_T$  extrapolation of the corrections, the uncertainty derived from the propagation of the single particle

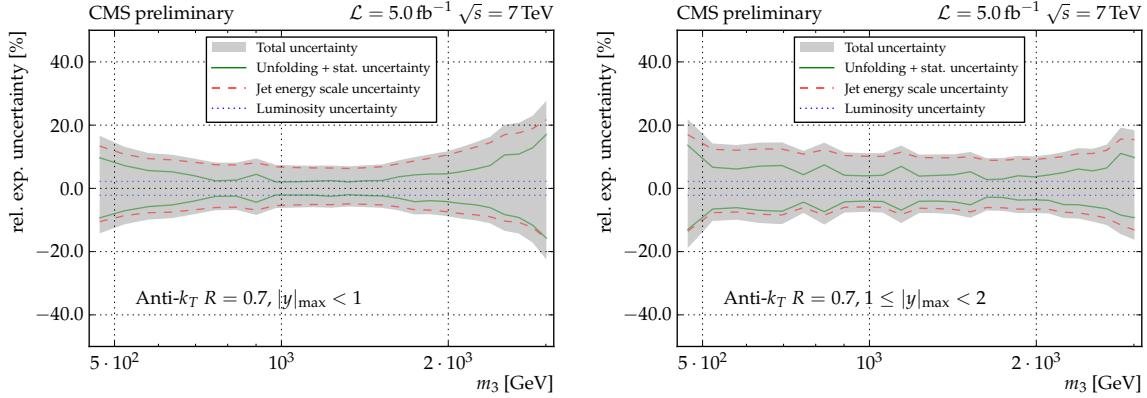


Figure 1: Overview of the measurement uncertainties in the innermost rapidity region  $|y|_{\text{max}} < 1$  (left) and in the outer rapidity region  $1 \leq |y|_{\text{max}} < 2$  (right).

response to particle flow jets, and the uncertainties on the corrections for pile-up collisions.

The luminosity uncertainty, which is fully correlated across all  $m_3$  and  $y_{\text{max}}$  bins, is estimated to be 2.2% [19].

Residual jet reconstruction and trigger inefficiencies are accounted for by an additional uncorrelated uncertainty of 1% like in Ref. [4].

Figure 1 presents an overview of the experimental uncertainties for the 3-jet mass measurement. Over a wide range of 3-jet masses, the jet energy scale uncertainty represents the largest contribution. At the edges of the investigated phase space, i.e. in the low and high 3-jet mass region, statistical and unfolding uncertainties, which are intrinsically linked through the unfolding procedure, become major contributors to the total uncertainty. Up to 3-jet masses of  $\approx 2 \text{ TeV}$ , the central rapidity bin exhibits a smaller total uncertainty than the outer rapidity bin.

## 5 Theory prediction

The theoretical predictions for the 3-jet mass cross sections consist of a NLO QCD calculation and a nonperturbative (NP) correction to account for the underlying event modelled by multiparton interactions (MPI) and for hadronization effects. Electroweak corrections to inclusive and dijet cross sections have been calculated in Ref. [20]. For 3-jet quantities these corrections are essentially unknown, but are not expected to be larger than in the dijet case, where the effect is limited to some percent at the highest dijet mass bins accessible with the CMS data from 2011 at 7 TeV center-of-mass energy.

The NLO calculations are performed using the NLOJET++ program version 4.1.3 [21, 22] within the framework of the FASTNLO package version 2.1 [23]. The renormalization and factorization scales,  $\mu_r$  and  $\mu_f$ , are identified with  $m_3/2$ . With this choice the NLO corrections to the LO cross sections, the  $K$  factors, remain limited between 1.2 and 1.6.

Comparisons to the NLO predictions are performed for five different PDF sets each with NLO and NNLO PDF evolutions. They are listed in Table 1 together with the corresponding number of active flavours  $N_f$ , the default values of the strong coupling constant  $\alpha_s(M_Z)$  and the ranges in  $\alpha_s(M_Z)$  available for fits. All PDF sets include a maximum of five active flavours  $N_f$  except for NNPDF2.1 which has  $N_{f,\text{max}} = 6$ . Only the ABM11 PDF set employs a fixed-flavour number scheme in contrast to variable-flavour number schemes favoured by all other PDF sets. For more details the respective references are given in Table 1.

Table 1: PDF sets used in comparisons to the data together with the corresponding number of active flavours  $N_f$ , the default values of the strong coupling constant  $\alpha_S(M_Z)$  and the ranges in  $\alpha_S(M_Z)$  available for fits. For CT10 the updated versions of 2012 are taken.

Base set	Reference(s)	Evol. order	$N_f$	$\alpha_S(M_Z)$	$\alpha_S(M_Z)$ variations
ABM11	[24]	NLO	5	0.1180	0.110–0.130
ABM11	[24]	NNLO	5	0.1134	0.104–0.120
CT10	[25]	NLO	$\leq 5$	0.1180	0.112–0.127
CT10	[25]	NNLO	$\leq 5$	0.1180	0.110–0.130
HERAPDF1.5	[26]	NLO	$\leq 5$	0.1176	0.114–0.122
HERAPDF1.5	[26]	NNLO	$\leq 5$	0.1176	0.114–0.122
MSTW2008	[27, 28]	NLO	$\leq 5$	0.1202	0.110–0.130
MSTW2008	[27, 28]	NNLO	$\leq 5$	0.1171	0.107–0.127
NNPDF2.1	[29]	NLO	$\leq 6$	0.1190	0.114–0.124
NNPDF2.1	[29]	NNLO	$\leq 6$	0.1190	0.114–0.124

Since most PDF sets have  $N_{f,\text{max}} = 5$ , this is also the default choice for the NLO predictions with NLOJET++, which considers all quarks to be massless. Theory calculations for jets at NLO with massive quarks do not exist at this time, such that only a consistency check with  $N_f = 6$  massless flavours in NLOJET++ is possible. If this is combined consistently with PDF sets made for up to six flavours, the resulting small effect should be contained within the NLO scale uncertainties. This has been tested with NNPDF2.1 and is found to be compatible.

For the NP corrections, the multi-jet improved Monte Carlo (MC) event generators SHERPA version 1.2.1 [30] and MADGRAPH 5 version 1.5.6 [31] are used to simulate 3-jet events. In the case of MADGRAPH the parton showering, MPI, and hadronization steps are taken over by PYTHIA8 version 8.149 [15, 32]. The 3-jet mass is determined for a given event before and after the MPI and hadronization phases are performed. This allows to derive correction factors which are applied to the theory prediction at NLO. The correction factor, which is defined as the center of the envelope covering the corrections of the two examined event generators above, ranges from 8% for the low mass range to about 1% at high 3-jet mass. The systematic uncertainty on the NP correction is estimated as  $\pm$  half of the spread between the two derivations, where usually SHERPA gives the smallest, and MADGRAPH 5 + PYTHIA8 the largest NP correction.

An overview of the different theoretical uncertainties is given in Fig. 2.

## 6 Results

Figure 3 compares the unfolded 3-jet mass distribution with the NLO prediction employing the MSTW2008-NLO PDF set and multiplying by the NP correction factor. It is observed that pQCD is able to describe the 3-jet mass cross section over five orders of magnitude and for 3-jet masses up to 3 TeV. To better judge potential differences between data and theory, the ratios of the measured cross sections to the theory predictions are presented in Fig. 4. Within uncertainties most PDF sets are able to describe the data. Small deviations are visible with the HERAPDF1.5 NLO set. Significant disagreements are exhibited by the ABM11 PDFs.

Although for most PDF sets there are no obvious deviations, the data are suitable to constrain the PDFs or to determine the strong coupling constant  $\alpha_S(M_Z)$ . In order to see where PDFs can

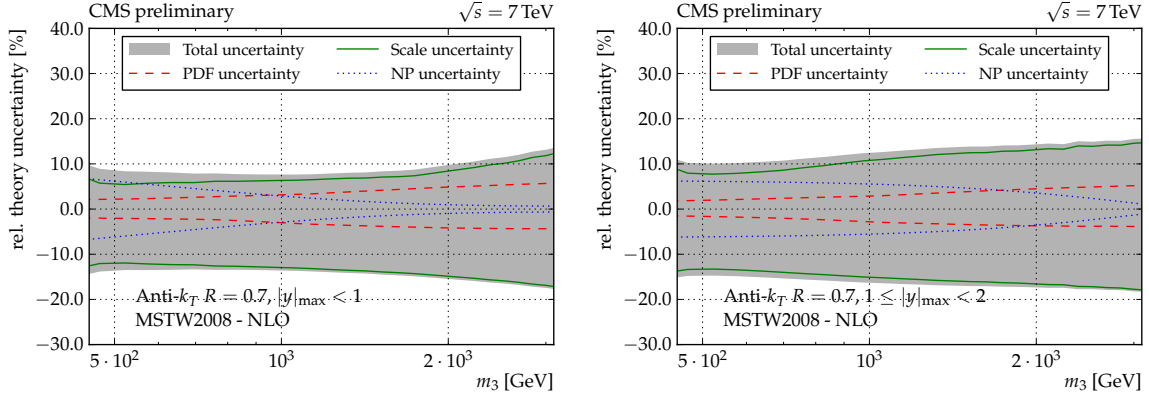


Figure 2: Overview of the theory uncertainties in the innermost rapidity region  $|y|_{\max} < 1$  (left) and in the outer rapidity region  $1 \leq |y|_{\max} < 2$  (right) for the MSTW2008 PDF set with NLO PDF evolution.

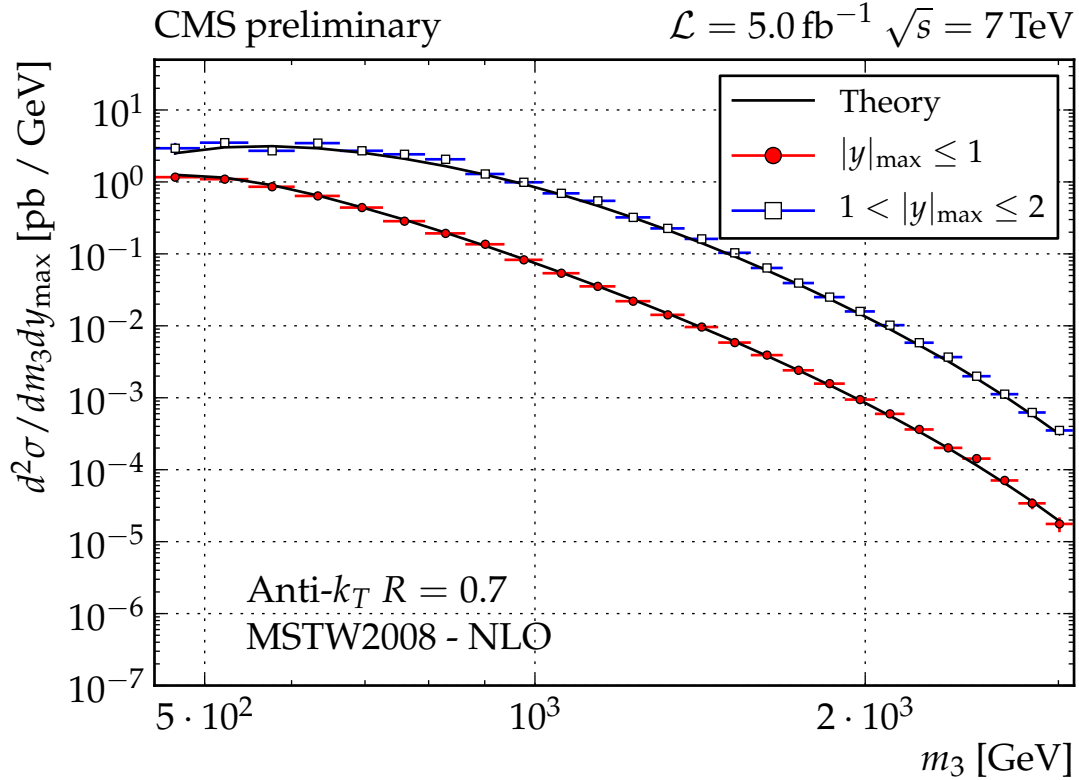


Figure 3: Comparison of the unfolded 3-jet mass cross section with the NLO prediction times NP corrections for the two considered regions in  $|y|_{\max}$  using the MSTW2008-NLO PDF set. The error bars represent the total experimental uncertainty.



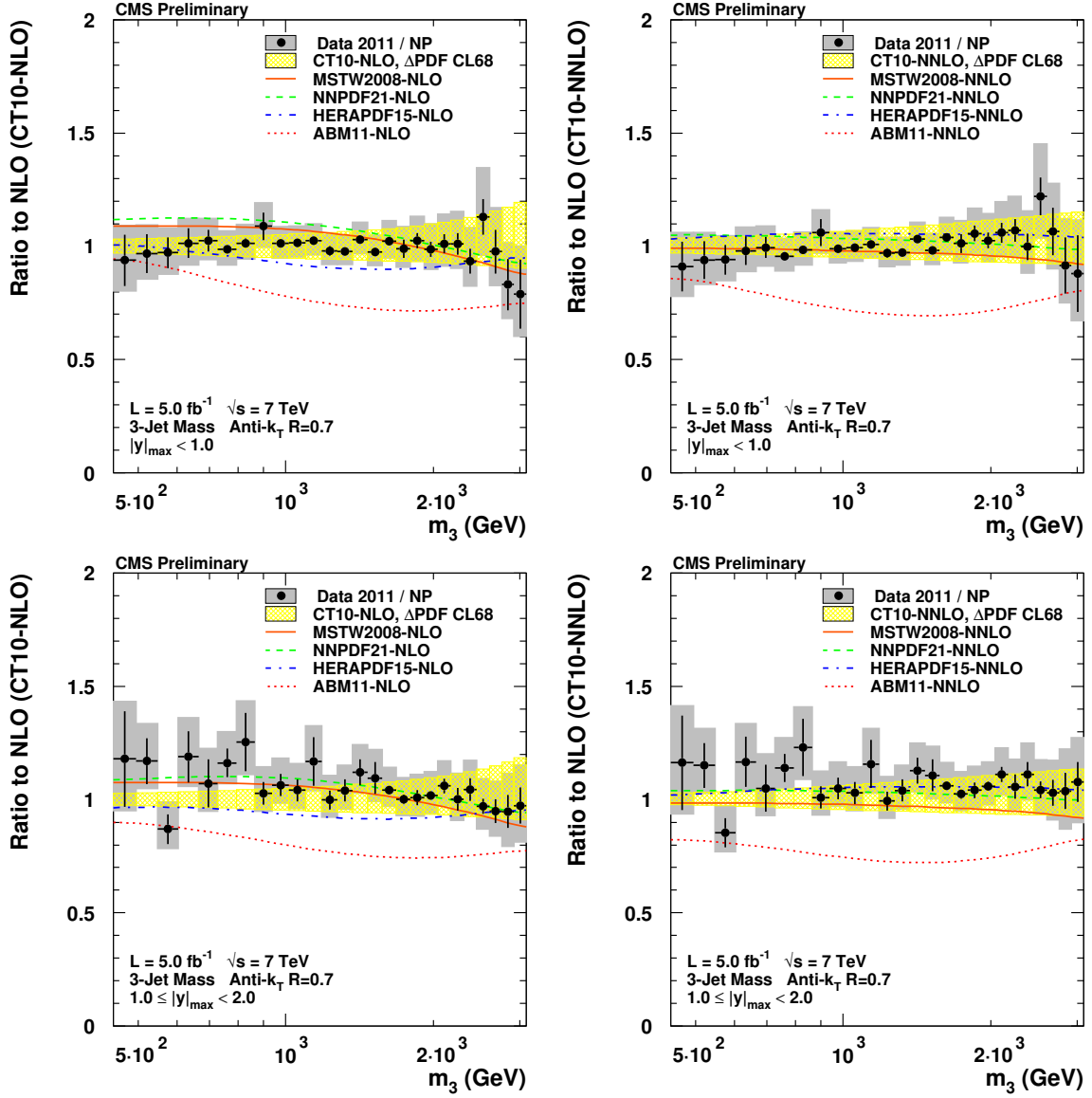


Figure 4: Ratio of the unfolded 3-jet mass distribution to the theory prediction including NP effects using PDF sets with NLO (left) or NNLO (right) PDF evolution in the inner rapidity bin  $|y|_{\max} < 1$  (top row) and the outer one  $1 \leq |y|_{\max} < 2$  (bottom row). The data are shown with error bars representing the statistical uncertainty and gray squares for the systematic uncertainties. The PDF uncertainty is shown for the CT10 PDF set at 68% confidence level as yellow band. In addition the central predictions are displayed for the other four examined PDF sets MSTW2008, NNPDF2.1, HERAPDF1.5, and ABM11.

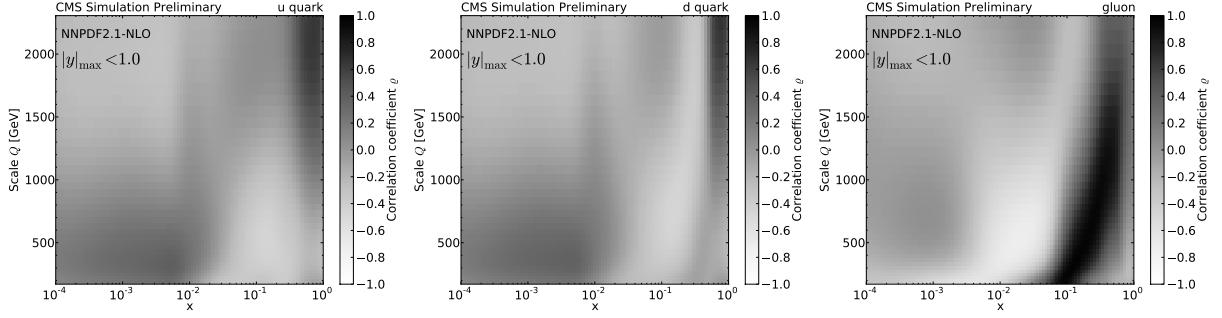


Figure 5: Correlation coefficient  $\rho_i(x, Q^2)$  between the 3-jet mass cross section  $\sigma_{m_3}(x, Q^2)$  and  $x$  times the parton distribution function  $f_i(x, Q^2)$  as derived from the replicas of the NNPDF2.1 PDF set. The correlation is presented for the up (left), down (middle) and gluon (right) parton distributions in the inner rapidity bin  $|y|_{\max} < 1$ .

be improved with 3-jet mass measurements, the correlation coefficients

$$\rho_i(x, Q^2) = \frac{N_{\text{rep}}}{(N_{\text{rep}} - 1)} \cdot \frac{\langle \sigma_{m_3}(x, Q^2) x f_i(x, Q^2) \rangle - \langle \sigma_{m_3}(x, Q^2) \rangle \langle x f_i(x, Q^2) \rangle}{\Delta_{\sigma_{m_3}(x, Q^2)} \Delta_{x f_i(x, Q^2)}} \quad (4)$$

can be investigated. Here, this is performed using the sampling method of the NNPDF2.1 set, where  $N_{\text{rep}}$  is the number of replicas,  $\sigma_{m_3}$  and  $f_i$  are the 3-jet mass cross section and the parton distribution function for parton flavour  $i$ , both dependent on the fractional parton momentum  $x$  and the relevant momentum scale  $Q = m_3/2$ .  $\Delta$  represents the standard deviation around the ensemble mean of  $\sigma_{m_3}(x, Q^2)$  and  $x f_i(x, Q^2)$  and the index  $i$  runs over all quark, anti-quark and gluon flavours. The resulting correlation coefficients are shown for the up- and down-quark, and the gluon in the inner rapidity bin  $|y|_{\max} < 1$  in Fig. 5 and demonstrate the potential impact at high  $x$ , in particular for the gluon between  $0.05 < x < 0.5$ . The correlations behave similarly in the outer rapidity bin.

In the following, the PDFs are considered as external input such that a value of the strong coupling  $\alpha_s(M_Z)$  can be ascertained. Potential correlations between  $\alpha_s(M_Z)$  and the PDFs are taken into account by using PDF sets including variations in  $\alpha_s(M_Z)$  as listed in table 1. Then, the value of  $\alpha_s(M_Z)$ , which shows the best compatibility can be determined by quantifying the difference between the measured distribution  $\sigma_{m_{3,i}}^{\text{data}}$  and the different theory predictions  $\sigma_{m_{3,i}}^{\text{theory}}(\alpha_s(M_Z))$  with a  $\chi^2$  test:

$$\chi^2 = \sum_{i,j=n_A}^{n_B} \left( \sigma_{m_{3,i}}^{\text{data}} - \sigma_{m_{3,i}}^{\text{theory}} \right) \left[ \text{cov}_{\text{sum}}^{-1} \left( \sigma_{m_{3,i}}, \sigma_{m_{3,j}} \right) \right] \left( \sigma_{m_{3,j}}^{\text{data}} - \sigma_{m_{3,j}}^{\text{theory}} \right), \quad (5)$$

where  $n_A$  and  $n_B$  are the bin indices specifying the 3-jet mass range. The total 3-jet mass covariance  $\text{cov}_{\text{sum}}$  is given as the sum of the covariances due to jet energy scale (JEC), the luminosity, unfolding and statistical uncertainties on the experimental side and the NP correction and PDF uncertainty on the theory side:

$$\text{cov}_{\text{sum}} = \text{cov}_{\text{JEC}} + \text{cov}_{\text{luminosity}} + \text{cov}_{\text{unfolding+stat}} + \text{cov}_{\text{NP}} + \text{cov}_{\text{PDF}}. \quad (6)$$

Here, the luminosity and NP corrections are considered as fully correlated between all  $m_3$  bins, while for the other uncertainties the corresponding experimental or theoretical recommenda-

Table 2: Determinations of  $\alpha_S(M_Z)$  in the considered  $m_3$  ranges for the inner rapidity bin. The relevant scale in each 3-jet mass range is calculated from the cross-section weighted average as given by the theory prediction using the MSTW2008 PDF set with NLO evolution. The overall fit is using the whole 3-jet mass range in the inner rapidity region. The quoted uncertainties are the combined uncertainty from experimental sources, the PDFs, and the NP corrections. The scale uncertainty is given separately.

$m_3$ [ GeV ]	$\langle Q \rangle$ [ GeV ]	$\chi^2/N_{\text{dof}}$	$\alpha_S(M_Z)$	$\pm(\text{exp,PDF,NP})$	$\pm(\text{scale})$
445–604	$258 \pm 12$	0.05/3	0.1152	$\pm_{0.0044}^{0.0042}$	$\pm_{0.0019}^{0.0053}$
604–794	$339 \pm 14$	0.28/3	0.1163	$\pm_{0.0034}^{0.0032}$	$\pm_{0.0022}^{0.0058}$
794–938	$427 \pm 12$	0.46/2	0.1179	$\pm_{0.0041}^{0.0042}$	$\pm_{0.0023}^{0.0063}$
938–1098	$502 \pm 13$	0.01/2	0.1177	$\pm 0.0039$	$\pm_{0.0024}^{0.0065}$
1098–1369	$600 \pm 20$	0.70/3	0.1174	$\pm_{0.0031}^{0.0032}$	$\pm_{0.0025}^{0.0066}$
1369–2172	$783 \pm 32$	2.22/7	0.1175	$\pm 0.0034$	$\pm_{0.0027}^{0.0085}$
2172–2602	$1163 \pm 31$	1.40/3	0.1218	$\pm_{0.0060}^{0.0037}$	$\pm_{0.0048}^{0.0061}$
2602–3092	$1386 \pm 34$	0.33/3	0.1166	$\pm_{0.0100}^{0.0075}$	$\pm_{0.0075}^{0.0088}$
445–3092	$304 \pm 15$	9.11/26	0.1160	$\pm_{0.0023}^{0.0025}$	$\pm_{0.0021}^{0.0068}$

tions for the determination of the correlations are applied. The fits are based on the innermost rapidity bin, which exhibits smaller uncertainties compared with the outer rapidity bin.

The scale uncertainty of the theory prediction is considered via separate fits for different scale settings as described below. In order to study the running of the strong coupling constant, the comparison between data and theory is performed also separately in several 3-jet mass regions as given in Table 2. The size of the regions is chosen such that a reasonable fit can be obtained and at least two 3-jet mass bins are included.

The MSTW2008-NLO PDF set is selected for the main result, since the large range in available  $\alpha_S(M_Z)$  values from 0.110 up to 0.130 in steps of 0.001 enables for all fits and scale variations to determine the minimum in  $\chi^2$  in all bins. The asymmetric uncertainty is determined by finding the  $\chi^2 + 1$  points of the curve.

The scale uncertainty is evaluated via the offset method, where the minimal and maximal deviations from the central result  $\mu_r = \mu_f = m_3/2$ , which are observed in six variations of the scale settings, are taken as uncertainty. The six variations are defined as the following scale factor combinations for the renormalization scale  $\mu_r$  and factorization scale  $\mu_f$ : (1/2,1/2), (1/2,1), (1,1/2), (1,2), (2,1), and (2,2).

In order to propagate the fitted value of  $\alpha_S(M_Z)$  back to the scale of the measurement,  $Q$ ,  $\alpha_S$  evolution code following Ref. [33] is employed.

For comparison, the fit was also performed for the alternative PDF sets CT10-NLO and NNLO, HERAPDF1.5-NLO and NNLO, MSTW2008-NNLO and NNPDF2.1-NLO and NNLO. The results are presented in table 3. Note that for the NNPDF2.1-NLO PDF set, the scale uncertainty had to be determined from an extrapolation of the  $\chi^2$  curve, since the provided set of  $\alpha_S$  variations was not sufficient. Such an extrapolation is not necessary for the MSTW2008-NLO PDF, which therefore was taken as the default in this study. As can be seen, the fit results on  $\alpha_S(M_Z)$  are in agreement between the investigated PDF sets and PDF evolution orders within uncertainties. Overall, the fits with different PDFs agree within uncertainties with each other.

Figure 6 shows the  $\alpha_S(Q)$  evolution as determined in this analysis with MSTW2008-NLO in comparison to the world average. The figure also shows an overview over the measurements

Table 3: Determinations of  $\alpha_S(M_Z)$  with different PDFs using the whole 3-jet mass range in the inner rapidity region. The quoted uncertainties are the combined uncertainty from experimental sources, the PDF uncertainty, and the NP corrections. The scale uncertainty is given separately. Note that for the NNPDF2.1-NLO PDF set, the scale uncertainty had to be determined from an extrapolation of the  $\chi^2$  curve.

PDF	$\chi^2/N_{\text{dof}}$	$\alpha_S(M_Z)$	$\pm(\text{exp, PDF, NP})$	$\pm(\text{scale})$
CT10-NLO	8.92/26	0.1169	$\pm_{0.0032}^{0.0031}$	$\pm_{0.0025}^{0.0059}$
CT10-NNLO	8.51/26	0.1164	$\pm 0.0028$	$\pm_{0.0022}^{0.0055}$
HERAPDF15-NLO	14.76/26	0.1200	$\pm 0.0014$	$\pm_{0.0010}^{0.0063}$
HERAPDF15-NNLO	9.00/26	0.1159	$\pm_{0.0011}^{0.0012}$	$\pm_{0.0007}^{0.0028}$
MSTW2008-NLO	9.11/26	0.1160	$\pm_{0.0023}^{0.0025}$	$\pm_{0.0021}^{0.0068}$
MSTW2008-NNLO	9.54/26	0.1167	$\pm_{0.0024}^{0.0026}$	$\pm_{0.0026}^{0.0059}$
NNPDF21-NLO	9.01/26	0.1140	$\pm_{0.0026}^{0.0027}$	$\pm_{0.0014}^{0.0049}$
NNPDF21-NNLO	9.47/26	0.1168	$\pm_{0.0024}^{0.0021}$	$\pm_{0.0018}^{0.0042}$

of the running of the strong coupling from various other experiments [34–40] together with recent determinations by CMS [41, 42] and from this analysis. Within uncertainties the new results presented here are in agreement with the world measurements and extend the covered range in scale  $Q$  up to a new record value of  $\approx 1.4$  TeV.

## 7 Conclusions

The proton-proton collision data collected by the CMS experiment in 2011 at a center-of-mass energy of 7 TeV were used to measure the double-differential 3-jet mass cross section. The cross section covers the 3-jet mass range from 0.45 TeV up to 3.1 TeV in two rapidity bins up to  $|y|_{\text{max}} = 2$ . Within the experimental and theoretical uncertainties, which are of comparable size, the data are in agreement with predictions of perturbative QCD at next-to-leading order except for calculations employing the ABM11 PDF set, where significant deviations are observed.

From the comparison between data and theory the strong coupling constant has been determined in multiple regions of 3-jet mass  $m_3$  at scales  $Q = m_3/2$  between 0.26 TeV and  $\approx 1.4$  TeV. The results are consistent with the evolution of the strong coupling as predicted by the renormalization group equation and with the world average on  $\alpha_S(M_Z)$ . They are also consistent with previous measurements from CMS comparing the 3-jet rate  $R_{32}$  to NLO predictions in a similar range of scales  $Q$  [41] or from determining the strong coupling at the top production threshold using theory at NNLO, which consequently leads to smaller scale uncertainties [42].

A combined fit of all data points gives the value of the strong coupling at the scale of the Z boson mass to be  $\alpha_S(M_Z) = 0.1160 \pm_{0.0023}^{0.0025} (\text{exp, PDF, NP}) \pm_{0.0021}^{0.0068} (\text{scale})$ . The results have been achieved at NLO perturbative QCD with the MSTW2008 PDF set at NLO evolution order. They are in agreement within uncertainties with fits using the alternative PDF sets CT10-NLO and NNLO, HERAPDF1.5-NLO and NNLO, MSTW2008-NNLO, and NNPDF2.1-NLO and NNLO.

## References

- [1] ATLAS Collaboration, “Measurement of inclusive jet and dijet cross sections in proton-proton collisions at 7 TeV centre-of-mass energy with the ATLAS detector”, *Eur.*

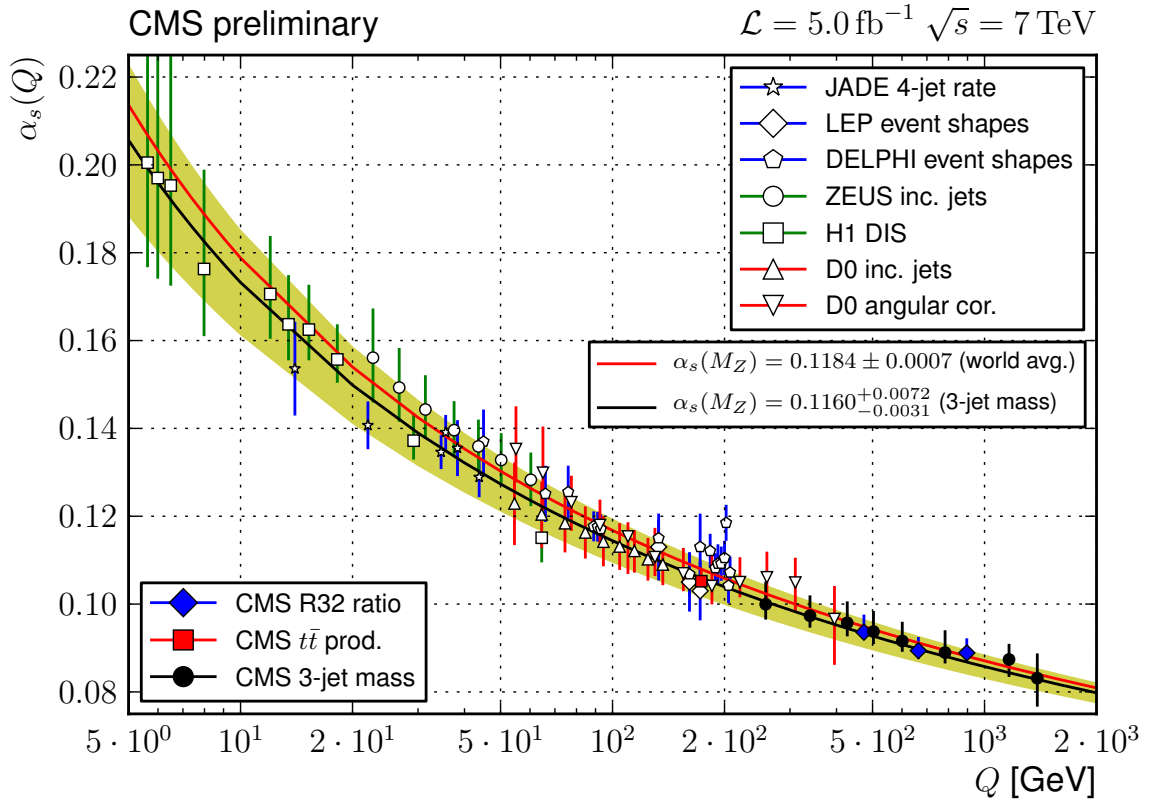


Figure 6: Comparison of the  $\alpha_s(Q)$  evolution as determined in this analysis from all measurement bins at central rapidity (curve with uncertainty band) to the world average (upper curve). The error bars on the data points correspond to the total uncertainty. In addition an overview of measurements of the running of the strong coupling constant  $\alpha_s(Q)$  from electron-positron collider experiments [38–40], electron-proton experiments [43–45], and proton/anti-proton collider experiments [34, 35, 41, 42] is presented. The results of this analysis extend the covered range to high scales  $Q$  up to  $\approx 1.4 \text{ TeV}$ .

- Phys. J. C* **71** (2011) 1512, doi:10.1140/epjc/s10052-010-1512-2, arXiv:1009.5908.
- [2] CMS Collaboration, “Measurement of the inclusive jet cross section in pp collisions at  $\sqrt{s} = 7$  TeV”, *Phys. Rev. Lett.* **107** (2011) 132001, doi:10.1103/PhysRevLett.107.132001.
- [3] CMS Collaboration, “Measurement of the differential dijet production cross section in proton-proton collisions at  $\sqrt{s} = 7$  TeV”, *Phys. Lett. B* **700** (2011) 187, doi:10.1016/j.physletb.2011.05.027.
- [4] CMS Collaboration, “Measurements of differential jet cross sections in proton-proton collisions at  $\sqrt{s} = 7$  TeV with the CMS detector”, *Phys. Rev. D* **87** (2012) 12002, doi:10.1103/PhysRevD.87.12002.
- [5] D0 Collaboration, “Measurement of three-jet differential cross sections  $d\sigma_{3\text{jet}}/dM_{3\text{jet}}$  in  $p\bar{p}$  collisions at  $\sqrt{s} = 1.96$  TeV”, *Phys. Lett. B* **704** (2011) 434, doi:10.1016/j.physletb.2011.09.048, arXiv:1104.1986.
- [6] CMS Collaboration, “The CMS experiment at the CERN LHC”, *JINST* **03** (2008) S08004, doi:10.1088/1748-0221/3/08/S08004.
- [7] CMS Collaboration, “Particle-Flow Event Reconstruction in CMS and Performance for Jets, Taus, and  $E_T^{\text{miss}}$ ”, CMS Physics Analysis Summary CMS-PAS-PFT-09-001, (2009).
- [8] CMS Collaboration, “Commissioning of the Particle-flow Event Reconstruction with the first LHC collisions recorded in the CMS detector”, CMS Physics Analysis Summary CMS-PAS-PFT-10-001, (2010).
- [9] M. Cacciari, G. P. Salam, and G. Soyez, “The anti- $k_t$  jet clustering algorithm”, *JHEP* **04** (2008) 063, doi:10.1088/1126-6708/2008/04/063, arXiv:0802.1189.
- [10] M. Cacciari, G. P. Salam, and G. Soyez, “FastJet user manual”, *Eur. Phys. J. C* **72** (2012) 1896, doi:10.1140/epjc/s10052-012-1896-2, arXiv:1111.6097.
- [11] CMS Collaboration, “Determination of Jet Energy Calibration and Transverse Momentum Resolution in CMS”, *JINST* **6** (2011) P11002, doi:10.1088/1748-0221/6/11/P11002, arXiv:1107.4277.
- [12] CMS Collaboration, “Tracking and Vertexing Results from First Collisions”, CMS Physics Analysis Summary CMS-PAS-TRK-10-001, (2010).
- [13] CMS Collaboration, “Calorimeter Jet Quality Criteria for the First CMS Collision Data”, CMS Physics Analysis Summary CMS-PAS-JME-09-008, (2010).
- [14] G. D’Agostini, “A Multidimensional unfolding method based on Bayes’ theorem”, *Nucl. Instrum. Meth. A* **362** (1995) 487, doi:10.1016/0168-9002(95)00274-X.
- [15] T. Sjöstrand, S. Mrenna, and P. Skands, “PYTHIA 6.4 Physics and Manual”, *JHEP* **05** (2006) 026, doi:10.1088/1126-6708/2006/05/026, arXiv:hep-ph/0603175.
- [16] R. Field, “Early LHC Underlying Event Data-Findings and Surprises”, (2010). arXiv:1010.3558v1. preprint.
- [17] The PYTHIA6 Z2 tune is identical to the Z1 tune described in [16] except that Z2 uses the CTEQ6L PDF while Z1 uses CTEQ5L.

- [18] M. Bähr et al., “Herwig++ Physics and Manual”, *Eur. Phys. J. C* **58** (2008) 639, doi:10.1140/epjc/s10052-008-0798-9, arXiv:0803.0883.
- [19] CMS Collaboration, “Absolute Calibration of the Luminosity Measurement at CMS: Winter 2012 Update”, CMS Physics Analysis Summary CMS-PAS-SMP-12-008, (2012).
- [20] S. Dittmaier, A. Huss, and C. Speckner, “Weak radiative corrections to dijet production at hadron colliders”, *JHEP* **1211** (2012) 095, doi:10.1007/JHEP11(2012)095, arXiv:1210.0438.
- [21] Z. Nagy, “Three-jet cross sections in hadron-hadron collisions at next-to-leading order”, *Phys. Rev. Lett.* **88** (2002) 122003, doi:10.1103/PhysRevLett.88.122003, arXiv:hep-ph/0110315.
- [22] Z. Nagy, “Next-to-leading order calculation of three jet observables in hadron hadron collision”, *Phys. Rev. D* **68** (2003) 094002, doi:10.1103/PhysRevD.68.094002, arXiv:hep-ph/0307268.
- [23] D. Britzger, K. Rabbertz, F. Stober, and M. Wobisch, “New features in version 2 of the fastNLO project”, doi:10.3204/DESY-PROC-2012-02/165, arXiv:1208.3641.
- [24] S. Alekhin, J. Blümlein, and S. Moch, “Parton Distribution Functions and Benchmark Cross Sections at NNLO”, *Phys. Rev. D* **86** (2012) 054009, doi:10.1103/PhysRevD.86.054009, arXiv:1202.2281.
- [25] H.-L. Lai et al., “New parton distributions for collider physics”, *Phys. Rev. D* **82** (2010) 074024, doi:10.1103/PhysRevD.82.074024, arXiv:1007.2241.
- [26] H1 and ZEUS Collaboration, “Combined Measurement and QCD Analysis of the Inclusive  $e^+p$  Scattering Cross Sections at HERA”, *JHEP* **1001** (2010) 109, doi:10.1007/JHEP01(2010)109, arXiv:0911.0884.
- [27] A. D. Martin, W. J. Stirling, R. S. Thorne, and G. Watt, “Parton distributions for the LHC”, *Eur. Phys. J. C* **63** (2009) 189, doi:10.1140/epjc/s10052-009-1072-5, arXiv:0901.0002.
- [28] A. Martin, W. Stirling, R. Thorne, and G. Watt, “Uncertainties on  $\alpha(S)$  in global PDF analyses and implications for predicted hadronic cross sections”, *Eur. Phys. J. C* **64** (2009) 653, doi:10.1140/epjc/s10052-009-1164-2, arXiv:0905.3531.
- [29] R. D. Ball et al., “Impact of Heavy Quark Masses on Parton Distributions and LHC Phenomenology”, *Nucl. Phys. B* **849** (2011) 296, doi:10.1016/j.nuclphysb.2011.03.021, arXiv:1101.1300.
- [30] T. Gleisberg et al., “Event generation with SHERPA 1.1”, *JHEP* **0902** (2009) 007, doi:10.1088/1126-6708/2009/02/007, arXiv:0811.4622.
- [31] J. Alwall et al., “MadGraph 5 : Going Beyond”, *JHEP* **1106** (2011) 128, doi:10.1007/JHEP06(2011)128, arXiv:1106.0522.
- [32] T. Sjöstrand, S. Mrenna, and P. Skands, “A Brief Introduction to PYTHIA 8.1”, *Comput. Phys. Commun.* **178** (2008) 852, doi:10.1016/j.cpc.2008.01.036, arXiv:0710.3820.

- [33] M. Glück, E. Reya, and A. Vogt, “Dynamical parton distributions revisited”, *Eur. Phys. J. C* **5** (1998) 461, doi:10.1007/s100520050289, arXiv:hep-ph/9806404.
- [34] D0 Collaboration, “Determination of the strong coupling constant from the inclusive jet cross section in  $p\bar{p}$  collisions at  $\sqrt{s}=1.96$  TeV”, *Phys. Rev. D* **80** (2009) 111107, doi:10.1103/PhysRevD.80.111107, arXiv:0911.2710.
- [35] D0 Collaboration, “Measurement of angular correlations of jets at  $\sqrt{s} = 1.96$  TeV and determination of the strong coupling at high momentum transfers”, *Phys. Lett. B* **718** (2012) 56, doi:10.1016/j.physletb.2012.10.003, arXiv:1207.4957.
- [36] ZEUS Collaboration, “Jet-radius dependence of inclusive-jet cross-sections in deep inelastic scattering at HERA”, *Phys. Lett. B* **649** (2007) 12, doi:10.1016/j.physletb.2007.03.039, arXiv:hep-ex/0701039.
- [37] H1 Collaboration, “Deep inelastic inclusive e p scattering at low x and a determination of  $\alpha_s$ ”, *Eur. Phys. J. C* **21** (2001) 33, doi:10.1007/s100520100720, arXiv:hep-ex/0012053.
- [38] JADE Collaboration, “Measurement of the strong coupling  $\alpha(s)$  from the four-jet rate in  $e^+e^-$  annihilation using JADE data”, *Eur. Phys. J. C* **48** (2006) 3, doi:10.1140/epjc/s10052-007-0226-6, 10.1140/epjc/s2006-02625-4, arXiv:0707.0392.
- [39] DELPHI Collaboration, “The Measurement of  $\alpha_s$  from event shapes with the DELPHI detector at the highest LEP energies”, *Eur. Phys. J. C* **37** (2004) 1, doi:10.1140/epjc/s2004-01889-x, arXiv:hep-ex/0406011.
- [40] S. Marti i Garcia, “Review of  $\alpha_s$  measurements at LEP-2”, arXiv:hep-ex/9704016.
- [41] CMS Collaboration, “Measurement of the ratio of the inclusive 3-jet cross section to the inclusive 2-jet cross section in  $pp$  collisions at  $\sqrt{s} = 7$  TeV and first determination of the strong coupling constant in the TeV range”, (2013). arXiv:1304.7498. Submitted to *Eur. Phys. J. C*.
- [42] CMS Collaboration, “Determination of the top-quark pole mass and strong coupling constant from the  $t\bar{t}$  production cross section in  $pp$  collisions at  $\sqrt{s} = 7$  TeV”, (2013). arXiv:1307.1907. Submitted to *Phys. Lett. B*.
- [43] H1 Collaboration, “Jet Production in ep Collisions at High  $Q^2$  and Determination of  $\alpha_s$ ”, *Eur. Phys. J. C* **65** (2010) 363, doi:10.1140/epjc/s10052-009-1208-7, arXiv:0904.3870.
- [44] H1 Collaboration, “Jet Production in ep Collisions at Low  $Q^2$  and Determination of  $\alpha_s$ ”, *Eur. Phys. J. C* **67** (2010) 1, doi:10.1140/epjc/s10052-010-1282-x, arXiv:0911.5678.
- [45] ZEUS Collaboration, “Inclusive-jet photoproduction at HERA and determination of  $\alpha_s$ ”, *Nucl. Phys. B* **864** (2012) 1, doi:10.1016/j.nuclphysb.2012.06.006, arXiv:1205.6153.